ELSEVIER

Polymer 40 (1998) 95–110

polymer

Scanning force microscopic investigation of plasticity and damage mechanisms in polypropylene spherulites under simple shear

G. Coulon[a,*], G. Castelein[a], C. G'Sell[b]

[a]LSPES, Université des Sciences et Technologies de Lille, Laboratoire de Structure et Propriétés de l'Etat Solide (URA CNRS 234), 59655 Villeneuve d'Ascq Cedex, France

[b]Ecole des Mines de Nancy, Laboratoire de Physique des Matériaux (URA CNRS 155), Parc de Saurupt, Nancy 54042, France

Received 9 January 1998; accepted 10 March 1998

Abstract

Plasticity and damage mechanisms have been investigated at the lamellar level by scanning force microscopy in bulk isotactic polypropylene under moderate applied shear stresses. The polypropylene under study contains both α and β spherulites. The SFM micrographs show clearly that the local mechanisms are basically the same for both α and β spherulites, but their intensity is much less lower in the α spherulites than in the β ones due to the presence of the daughter lamellae in the former case. The main deformation mechanisms which have been observed are: (i) kinking of the lamellae which lie along the principal compressive axis; (ii) nanocracks across the lamellae lying along the principal tensile axis; (iii) fragmentations of the lamellae which are parallel to the shear axis; (iv) fragmentations of the lamellae which are perpendicular to the shear axis.

Keywords: Scanning force microscopy; Semi-crystalline polymers; Plastic deformation mechanisms

1. Introduction

The morphology of bulk semicrystalline polymers cooled from the melt can be described by the following structural hierarchy: (i) crystal lamellae of folded chains, (ii) stacks of almost parallel crystal lamellae, each crystal separated by a thin, amorphous interlayer and (iii) supermolecular polycrystalline structures, e.g. spherulites, axialites or 'shish-kebabs' [1]. The characteristic scales of that heterogeneous morphology lie typically within the 10 nm–100 μm range. Since plasticity and damage properties in polymers are strongly influenced by their microstructure, it is obvious that, in the case of semicrystalline polymers, the understanding of the macroscopic mechanical behaviour requires to identify and analyse the plasticity and damage mechanisms which occur at the different characteristic levels mentioned above [2,3].

In the specific case of isotactic polypropylene, the morphology is even more complex: in a given range of temperature of crystallization, two kinds of supermolecular structures usually coexist: the monoclinic α spherulites and the hexagonal β ones [4,5].

In past years, much experimental work has been devoted to the mechanical behaviour of bulk semicrystalline polymers and elementary deformation mechanisms have been proposed [6–10]; however, most of those studies have been focused on the behaviour of high-density polyethylene. In many cases, evidence of the mechanisms has been obtained by indirect experimental techniques such as x-ray diffraction and birefringence [11–16]. In contrast with the case of single crystals and melt cast films [17–19], only few direct observations have been obtained on bulk samples by TEM [20,21], by SEM [22] or by SFM [23–25]. In the later case, most of the experiments have been performed on ultradrawn oriented polymers in order to visualize the nanofibrils [23,24]; little attention has been paid to clarify the local deformation mechanisms which occur at yield in the crystalline part of bulk semicrystalline polymers [26].

In the case of bulk isotactic polypropylene, only few papers have dealt with the local deformation mechanisms which take place in the crystalline part during the first steps of plastic deformation: most of the studies have reported on the global macroscopic mechanical behaviour [27]. In the past, the yielding behaviour of isotactic polypropylene has been studied in terms of plasticity mechanisms through a thermodynamic and kinetic analysis of yielding; however, no direct evidence of those mechanisms has been shown

* Corresponding author.

0032-3861/98/$ - see front matter
PII: S0032-3861(98)00221-3

[28,29]. Recently, the plastic deformation modes have been imaged at the spherulitic level by in situ scanning electron microscopy in bulk isotactic polypropylene under uniaxial tension and simple shear [22]. In that work, it has been shown that, under tensile loading, the α spherulites are brittle while the β ones are ductile up to large strains (25%). In contrast, under shear stress, both the α and β spherulites can undergo large plastic deformation, but the α spherulites deform about less than 25% than the whole specimen. To understand that difference, investigations at the lamellar level inside each type of spherulite are necessary. To our knowledge, up to now, no direct image of the plasticity and damage mechanisms has been published at the lamellar level in any semicrystalline polymer.

In the last years, scanning force microscopy [30–33] has been shown to be a promising technique for imaging directly smooth polymer surfaces from the microscopic level to the nanoscopic one. Scanning force microscopy is a non-destructive technique which is operated directly on the surface in air: it is thus easier to use than the replication technique. The original microscope was operating only in the contact mode (the tip being in permanent contact with the surface) [34]. That mode is not suitable for imaging the surface of bulk deformed isotactic polypropylene, since the pronounced relief of such surfaces enhances the frictional force and the resolution is poor. In the Tapping™ mode, the tip touches the surface intermittently [35] and there is no frictional force. Hence, the crystalline lamellae (20 nm in thickness) can be imaged easily even on rough surfaces [26,36].

In the present paper, our aim is to identify the plasticity and damage mechanisms which occur in bulk isotactic polypropylene under moderate applied shear stresses, i.e. during the first steps of plasticity. Simple shear has been chosen because, in this mode, there is no hydrostatic stress; as a consequence, no wide-spread cavitation is expected and intralamellar plastic shear is favoured. The polypropylene under study contains both α and β spherulites, the size of which is about 100 μm. SFM is used here to investigate the plasticity and damage mechanisms which take place at the lamellar level inside each kind of spherulite.

2. Material and techniques

2.1. iPP samples

The iPP was manufactured by Appryl (France). It is characterized by a broad molecular weight distribution as assessed by gel permeation chromatography with M_n = 75 940 g/mol and M_w = 262 000 g/mol. The iPP pellets were processed by intrusion in a thick mould designed for producing parallelepipedic iPP plates (300 × 200 × 15 mm). The intrusion process consists in slowly extruding the melt (whose initial temperature is 230°C) in a mould kept at 30°C and continuing the mould feeding under the extruding pressure (6 MPa) during the cooling sequence (cooling time = 240 s). The cooling kinetics is slow enough to ensure a reproducible semi-crystalline structure. Such intruded plates have no detectable orientation and possess much less chain degradation than injected ones. Due to the temperature gradient between the two external surfaces, the crystallization kinetics varies across the thickness of the plates and Aboulfaraj et al. [37] have shown that the spherulitic structure is thickness dependent. In the mid-thickness of the intruded plates, both α and β spherulites are present, the fraction of β-spherulites is ~60 vol.% and their mean size is 120 μm, while their fraction is 0% at the external surfaces of the plates [26,37].

The iPP samples were cut out of the central area of the plates; they have a parallelepipedic shape with a longitudinal notch 5 mm deep and 4 mm wide (Fig. 1). L, d and e are the dimensions of the calibrated part and their values are given in Fig. 1. This geometry favours the localization of plastic deformation within the predefined plane at the root of the notch.

The flat surface has been polished with several emery papers and finally with a very fine alumina powder (0.05 mm) until no residual scratch was visible. To enhance the presence of the crystalline phase, the samples were immersed for some time at room temperature in an acid solution (1.3 wt.% $KMnO_4$, 32.9 wt.% H_3PO_4 and 65.8 wt.% H_2SO_4) which etches preferentially the amorphous phase [38]. Subsequently, the samples were rinsed in a dilute H_2SO_4 solution, in hydrogen peroxide, in distilled water and in acetone; finally, they were dried in a vacuum oven. To compare our data to the previous SEM micrographs [22], the acid attack procedure has been used before the shear test for 40 min. This etching time corresponds to the minimum time necessary to get a good, homogeneous lamellar resolution by SFM; i.e. the whole amorphous phase is removed from the top surface by the acid attack and the crystalline lamellae can be imaged through the topographic contrast.

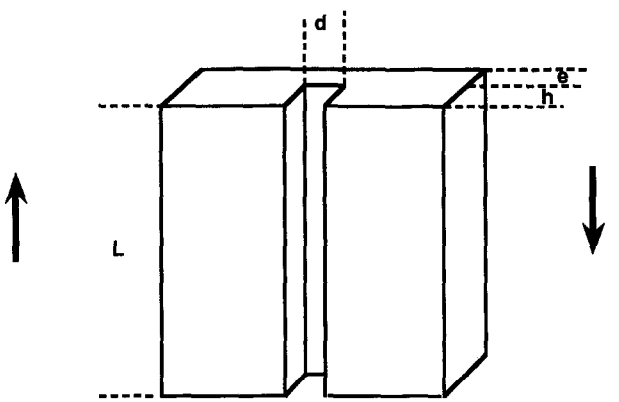

Fig. 1. Geometry of the samples used for simple shear test. L = 70 mm, d = 4 mm, e = 2 mm and h = 5 mm. The black arrows indicate the shear axes.

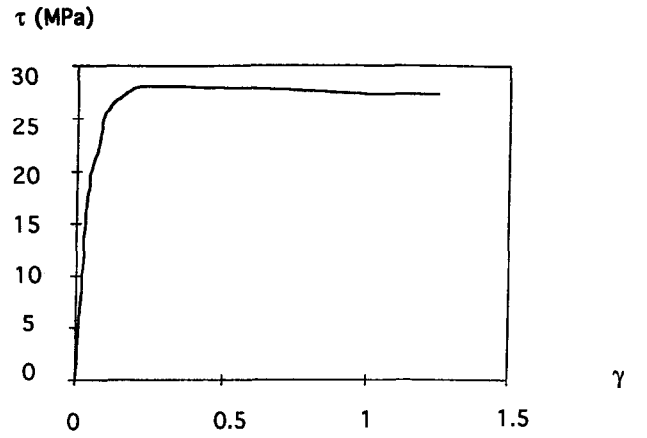

Fig. 2. A typical stress–strain curve of iPP samples deformed under simple shear stress at room temperature with a strain rate of $5 \times 10^{-4}\ s^{-1}$.

2.2. Simple shear tests

Simple shear tests were performed in a servo-hydraulic testing machine at room temperature with a true strain rate $\dot{\gamma}$ of $5 \times 10^{-4}\ s^{-1}$. The local shear strain has been measured by using a computed-assisted video-monitored extensometer [39]; this system was designed in such a way that the true shear rate can be controlled locally. A typical experimental stress–strain curve $\tau(\gamma)$ is shown in Fig. 2. The samples have been sheared up to a strain level which was about 30% greater than the desired one. Then, they were maintained under constant stress during 15 min and, finally, unloaded at the same strain rate $\dot{\gamma}$ of $5 \times 10^{-4}\ s^{-1}$. This procedure has been used in order to take account into the strong relaxation of the amorphous phase which behaves as an elastomer at room temperature. Two actual applied shear strain levels have thus been studied: $\gamma = 0.5$ and 1.

The morphology of both α and β spherulites at the surface of the sheared samples is shown in Fig. 3 for $\gamma = 0.5$ and 1. It is clear that, at the macroscopic scale, the deformation is homogeneous. As the shear strain level increases, both spherulites become more and more elongated along the principal tensile strain axis. The original equiaxed spherulites proceed to a nearly ellipsoidal shape which is similar to the deformation ellipsoid. The principal tensile strain axis coincides with the major axis of the ellipse and the principal compressive strain axis with the minor axis of the ellipse. In Fig. 4, the principal deformation axes of the simple shear test are given.

2.3. Scanning force microscopy experiments

SFM experiments were conducted on a Nanoscope III scanning force microscope (Digital Instruments). Measurements were carried out in the Tapping™ mode [35]. In that mode, the cantilever is forced to oscillate at a frequency (331 kHz) close to its resonance frequency with an adjustable amplitude. Its principle is given in Fig. 5. The tip contacts briefly the surface of the sample at each low position of the cantilever, the frictional force being thus eliminated. Pure monocrystalline silicon tips (model TESP), with a radius of curvature of about 10 nm, were used to image the surface. When the tip comes into contact with the surface, the atoms of the tip interact with the atoms of the surface in a repulsive way and the amplitude of the oscillation varies. The surface of the sample can be imaged in two different ways. 'Height' images are obtained by using the

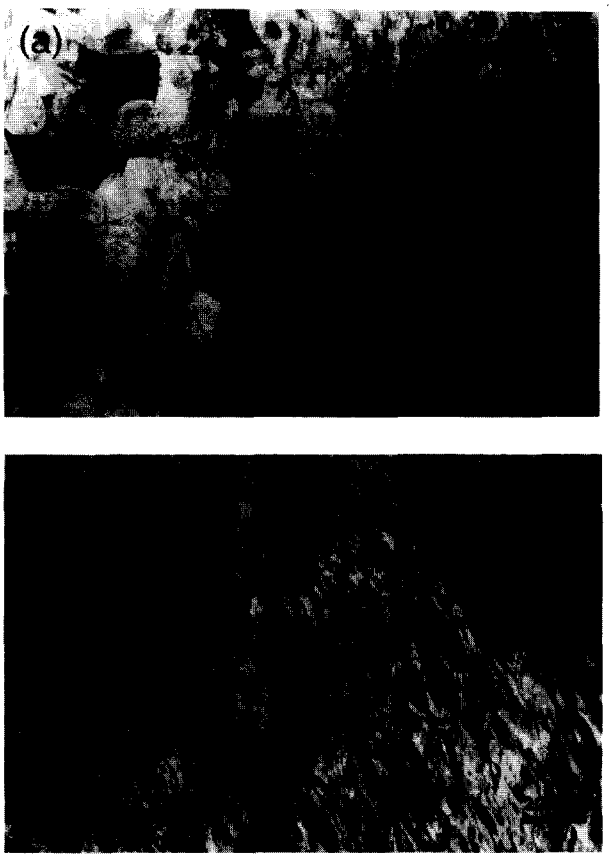

Fig. 3. Morphology of both α and β spherulites in iPP samples sheared at: (a) $\gamma = 0.5$ and (b) $\gamma = 1$, as revealed by optical microscopy. The black spherulites are β, while the white spherulites are α [26,37]. The shear axes ↑ ↓ are vertical.

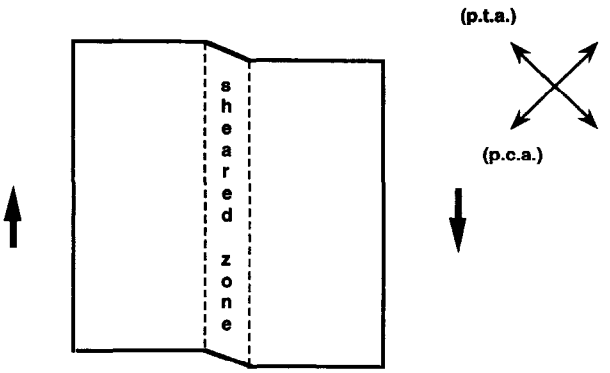

Fig. 4. Schematic top view of a sheared sample, the black arrows indicate the shear axes. The principal tensile strain axis (p.t.a.) and the principal compressive axis (p.c.a.) are shown.

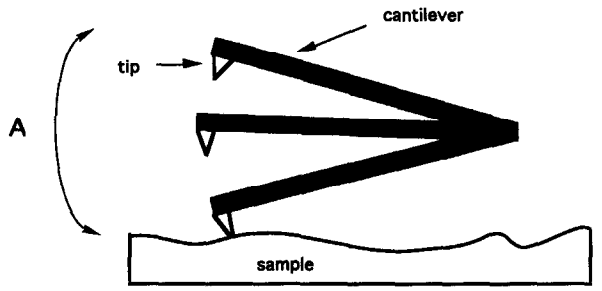

Fig. 5. Principle of the Tapping mode™. The tip is attached to a cantilever which is forced to oscillate at a high frequency with an adjustable amplitude A.

feedback loop which maintains the amplitude at a constant value by translating vertically the piezoelectric scanner; height measurements (z) are deduced from the vertical displacement (z) of the piezoelectric scanner and the image reflects the topography of the sample surface. 'Amplitude' images are obtained when the feedback loop is not connected; the amplitude can vary and the image corresponds to its variation. Since we were interested in the surface topology, all the images shown here are 'Height' images, they have been obtained by using either the (10 × 10 μm) or the (200 × 200 μm) scanner. The scanning frequency was about 1 Hz and the mean value of the repulsive normal force was of the order of 0.1 nN. All the images have been filtered through the 'Planefit' procedure [35].

3. Original crystalline microstructure in the undeformed state

3.1. Lamellar morphology of β spherulites

The lamellar morphology of the β spherulites has been observed in the equatorial plane of the 3D-spherulites. The morphology consists of broad, locally parallel stacked radial lamellae, just as in the spherulites of other polymers, as shown in Fig. 6. SFM images obtained along the same radial direction of α spherulite show that, apart from the central part, stacks of lamellae tend to twist along the radial growth direction and present a broad spread of orientations varying from **b**-axis (edge-on lamellae) to **c**-molecular axis (flat-on ones) profiles. In addition, splaying out of the lamellae is observed far from the core of the spherulite [26,36]. In flat-on views (Fig. 6b), the lamellae appear either rounded or faceted and numerous hexagonal etch terraces are visible, indicating that possibly screw dislocation growth mechanisms are operative [1,19,40,41].

The lamellar thickness can be deduced from the measurement of the interlamellar spacing; the interlamellar distances can be obtained through a 2D-section. As an example, Fig. 7 shows the SFM image of edge-on lamellae with its 2D-section along an axis perpendicular to the lamellae orientation. From the section profile, it is clear that the lamellae are perpendicular to the surface. One

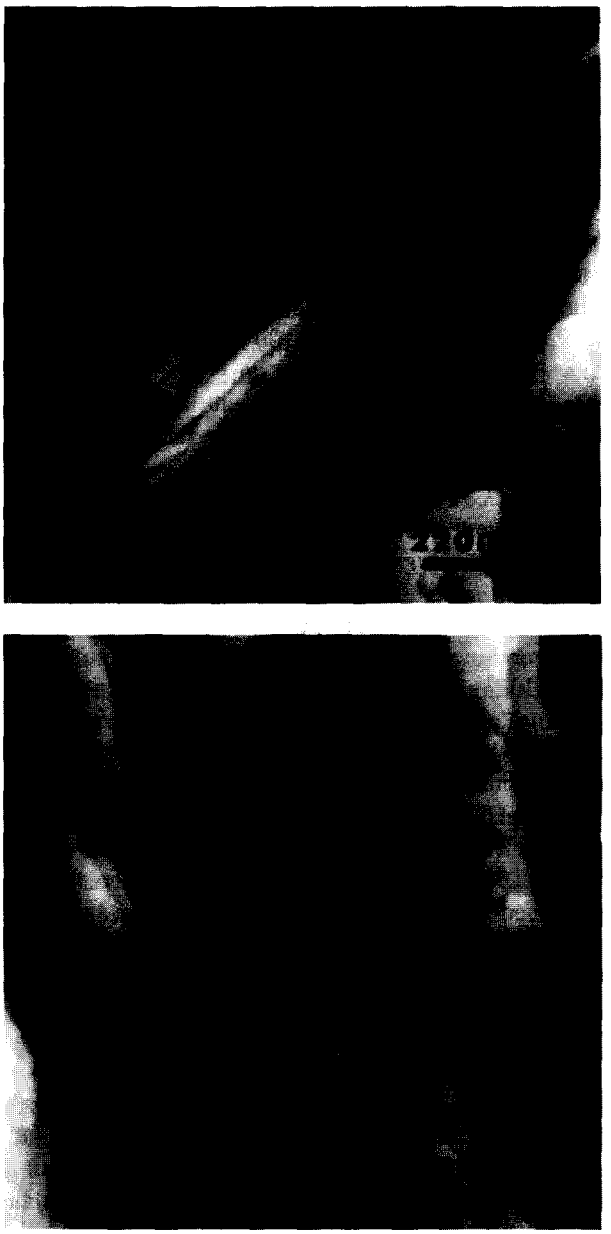

Fig. 6. Undeformed iPP samples: SFM images of the lamellae in β spherulites. (a) (2 × 2 μm) image of edge-on lamellae; z-range = 400 nm. (b) (1.5 × 1.5 μm) image of flat-on lamellae; z-range = 500 nm.

way to obtain the lamellar thickness could be to measure at the half-height the width of the lamellar peak. However, the width depends strongly on both the acid attack and the tip convolution (the curvature radius of the tip is about 10 nm, i.e. half the lamellar thickness) and the error bars would thus be large. A more accurate way to obtain the lamellar thickness is to measure the interlamellar spacing, i.e. the distance between two consecutive maxima of the lamellar profile since it does not depend on either the acid attack or the tip convolution. So doing, the mean-averaged value of the interlamellar distance is found to be 33.7 ± 8.3 nm. The degree of crystallinity has been measured elsewhere [37], it is equal to 66%. Thus, the lamellar thickness

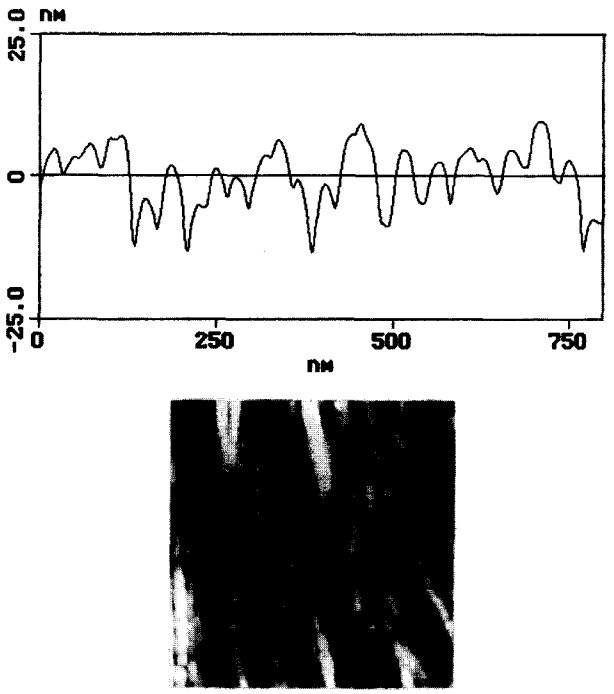

Fig. 7. Undeformed iPP samples: SFM images of the edge-on lamellae in β spherulites. Top: 2D-section of the image along an axis perpendicular to the lamellae orientation. Bottom: the corresponding SFM image.

represents 66% of the interlamellar spacing (amorphous layer + lamella) and its value is 22.2 ± 5.4 nm.

The lamellar thickness can also be obtained from the 2D-section of nearly flat-on lamellae views as shown in Fig. 8. The steps seen in the 2D-section correspond to the interlamellar spacings. Through geometrical considerations, it is easy to deduce the mean-averaged value of the interlamellar spacing: 36.8 ± 12.2 nm [42]. The error (± 12.2 nm) results from the difficulty in putting the cursor exactly at the top of the lamellae. Since the degree of crystallinity is equal to 66%, the mean-averaged value of the lamellar thickness is thus 24.3 ± 8.0 nm; this value is in good accordance with the one found in the case of edge-on lamellae.

From the observation of flat-on lamellae, it is also possible to estimate the width of the lamellae which is about 1 μm. Because of the limited field of view of the microscope, it is not possible to measure the length of the lamellae since they can grow from the core to the periphery of the spherulite.

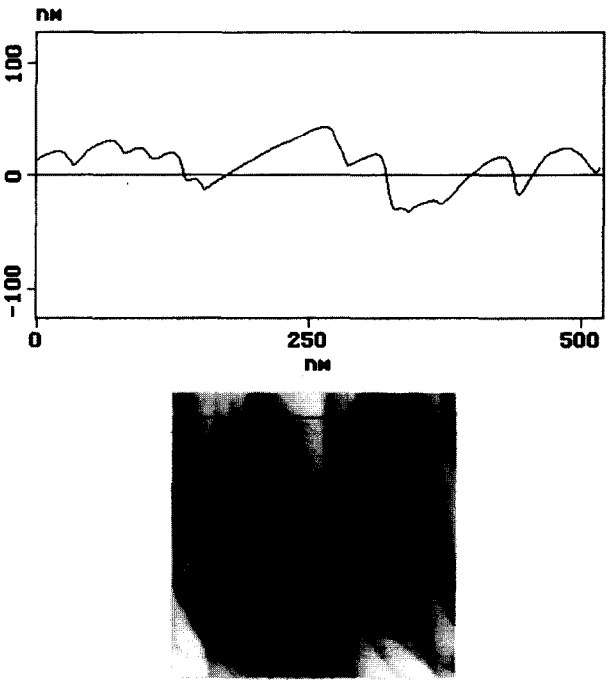

Fig. 8. Undeformed iPP samples: SFM images of the inclined lamellae in β spherulites. Top: 2D-section of the image along the axis shown on the SFM image. Bottom: the corresponding SFM image.

3.2. Lamellar morphology of α spherulites

In contrast with the β spherulites, the α spherulites contain two families of lamellae: the radial ones and the tangential (or daughter) ones [26,36]. SFM images (600 × 600 nm) obtained in any area of the spherulite show that the number of daughter lamellae is very high and quite constant from the core to the periphery of the spherulite. As mentioned earlier by Norton and Keller [41], the texture appears 'nodular' rather than lamellar because of the large number of daughter lamellae (Fig. 9); the 'nodules' correspond to the cross-hatched branchings. Typical (2 × 2 μm) SFM images show that, when progressing outward from the centre of the spherulite, the radial lamellae tend to splay out [26,36]. It has to be noted that, at this large scale (2 × 2 μm), the surface relief is more pronounced

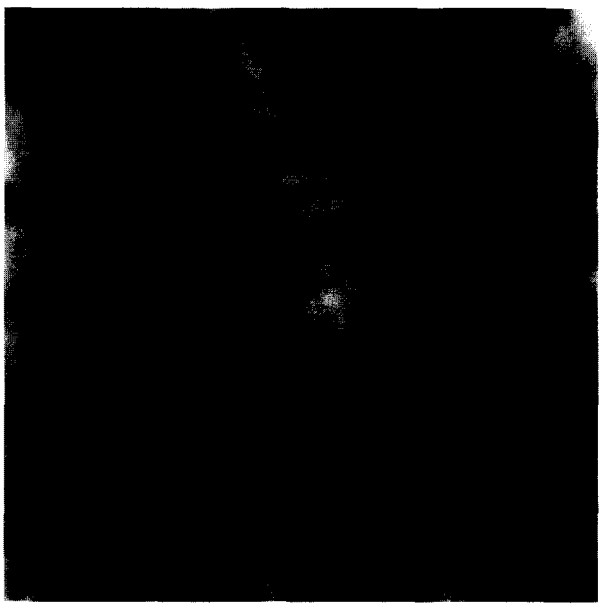

Fig. 9. A (600 × 600 nm) SFM image obtained on the surface of an undeformed iPP sample: the characteristic'nodular' structure of a α spherulite; z-range = 100 nm.

and the daughter lamellae cannot be resolved everywhere. Nevertheless, it has been possible to obtain the value of the angle between the radial and daughter lamellae by measuring it from a large number of those large scale images [42]: its value is 80 ± 10° which is in good agreement with the theoretical value (80°40′) found by Khoury [43]. Due to the cross-hatched structure, it has not been possible to deduce the value of the lamellar thickness from the 2D-section of the SFM images; indeed, the 2D-section profiles do not exhibit distinct and equidistant lamellar peaks because of the large number of branchings. Thus, the lamellar thickness has been measured directly on the SFM image for both radial and daughter lamellae. The measurements have been performed on a large number of images and the mean-averaged values are, for the radial lamellae, 21.8 ± 4.3 nm, and for the daughter ones, 18.5 ± 4.3 nm [42]. The radial lamellae are thus slightly thicker than the daughter ones; this result agrees with previous studies [41].

3.3. Synthesis

Referring to the Padden and Keith classification [5], the lamellar morphologies which have been observed here by SFM in both spherulites correspond to the α_I and β_{IV} types: (1) α_I type, dense network of radial and daughter lamellae; (2) β_{IV} type, radial twisted lamellae.

In isothermally crystallized thin films [5], α_I and β_{IV} spherulites occur at about 130°C. Consequently, the crystalline morphology observed in the mid-plane of the intruded iPP plates corresponds to what is found in thin films isothermally crystallized at about 130°C.

Fig. 10 shows the 3D-schematic lamellar morphologies of both α_I and β_{IV} spherulites [44,45].

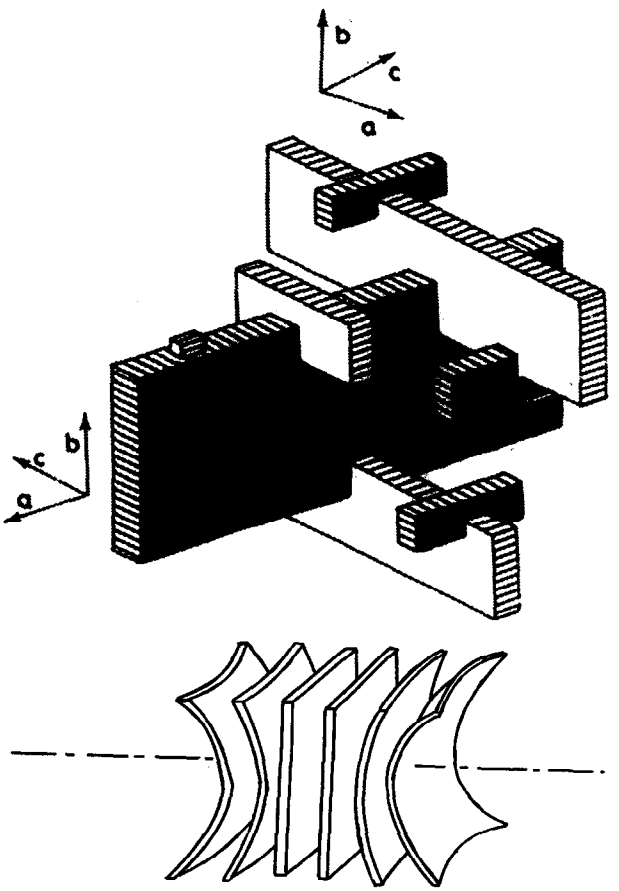

Fig. 10. 3D schematic lamellar morphologies of both α_I and β_{IV} spherulites. (a) α_I spherulites as proposed by Lotz and co-workers; (b) β_{IV} spherulites similar to the spherulites of other polymers [44].

4. Evolution of the lamellar morphology in sheared polypropylene

4.1. Introduction

As shown in Fig. 3, for $\gamma = 0.5$ and 1, the deformation is homogeneous at a macroscopic scale. As the shear strain level increases, both spherulites become more and more elongated along the principal tensile strain axis. Recently, in situ scanning electron microscopy experiments performed on bulk isotactic polypropylene under simple shear [22] have shown that the plastic deformation is quasi-affine at the spherulitic level. Both the α and β spherulites can undergo large plastic deformation; however, the α spherulites deform about 25% less than the overall specimen while the β spherulites are more ductile and override the average deformation of the sample by about 25%.

Here, our aim is to characterize the deformation mechanisms at the lamellar level inside both kinds of spherulites. A series of SFM observations have been performed on sheared samples for both shear levels $\gamma = 0.5$ and 1. Because of the heterogeneous morphology of both spherulites, the SFM images could not be scanned randomly on the surface; the location of the scanned areas have been chosen relatively to the centre of the spherulite and to the principal deformation axes. Only the data corresponding to a shear strain $\gamma = 1$ are shown here since the intensity of the deformation mechanisms is greater than for $\gamma = 0.5$ [26].

4.2. Lamellar morphology in deformed β spherulites

Fig. 11 shows four different lamellar morphologies corresponding to four different deformation states relative to the deformation ellipsoid.

In Fig. 11a, the lamellae are oriented along the shear axis. Along this axis, occurrence of interlamellar shear is expected in the amorphous phase; no direct trace of this mechanism is visible, this is because the SFM observation is performed after unloading the sample. The salient feature is the presence of numerous fragmentations of the crystalline lamellae; inside the lamellae, the fragmentations occur along the chain axis. It should be pointed out that, at a lower shear strain ($\gamma = 0.5$), there are only very few erratic fragmentations [26].

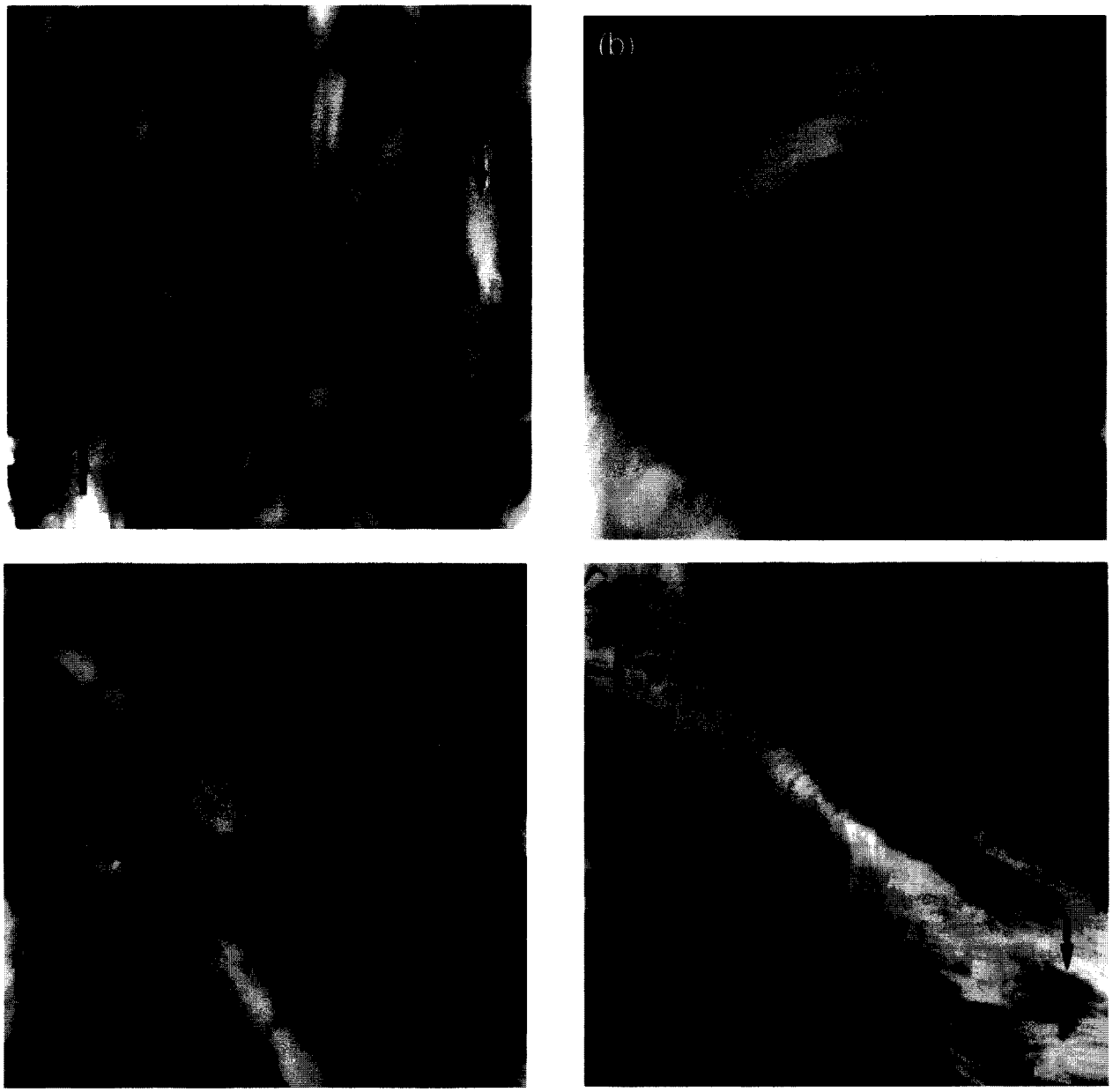

Fig. 11. iPP samples sheared at $\gamma = 1$: SFM images of the lamellar morphology in β spherulites. (a) The lamellae are parallel to the shear axis; (2×2 μm) image, z-range = 400 nm. (b) The lamellae are perpendicular to the shear axis; (2×2 μm) image, z-range = 800 nm. (c) The lamellae are parallel to the principal tensile axis; (5×5 μm) image, z-range = 1.2 μm. (d) The lamellae are parallel to the principal compressive axis; (5×5 μm) image, z-range = 1.3 μm. The black arrows indicate the shear axes.

When the lamellae are perpendicular to the shear axis (Fig. 11b), intralamellar slip should prevail since the crystalline slip planes are parallel to the shear axis. Nevertheless, no intralamellar slip is seen, but numerous fragmentations of the lamellae are present. For $\gamma = 0.5$, the lamellae are not fragmented and look like those in the undeformed state [26].

In areas where the lamellae are parallel to the principal tensile axis, at $\gamma = 0.5$, few cooperative nanocracks go through stacks of edge-on and flat-on lamellae as well, the nanocracks are perpendicular to the tensile axis. When increasing the applied shear strain at $\gamma = 1$, the number of collective nanocracks increases dramatically (Fig. 11c) and, incidentally, the stacks of lamellae which are parallel to the principal tensile axis are broken into smaller blocks.

When the lamellae lie along the principal compressive axis, at $\gamma = 0.5$, few local kinks of the lamellae are observed [26]. At $\gamma = 1$, the lamellar kinkings become cooperative and give rise to the formation of kink bands perpendicular to the principal compressive axis (Fig. 11d).

Indeed, all the situations shown in Fig. 11 are characteristic of the equatorial plane of the spherulite (as mentioned above in Section 3.1) which is perpendicular to the shear plane. However, the local shear stress is different in any

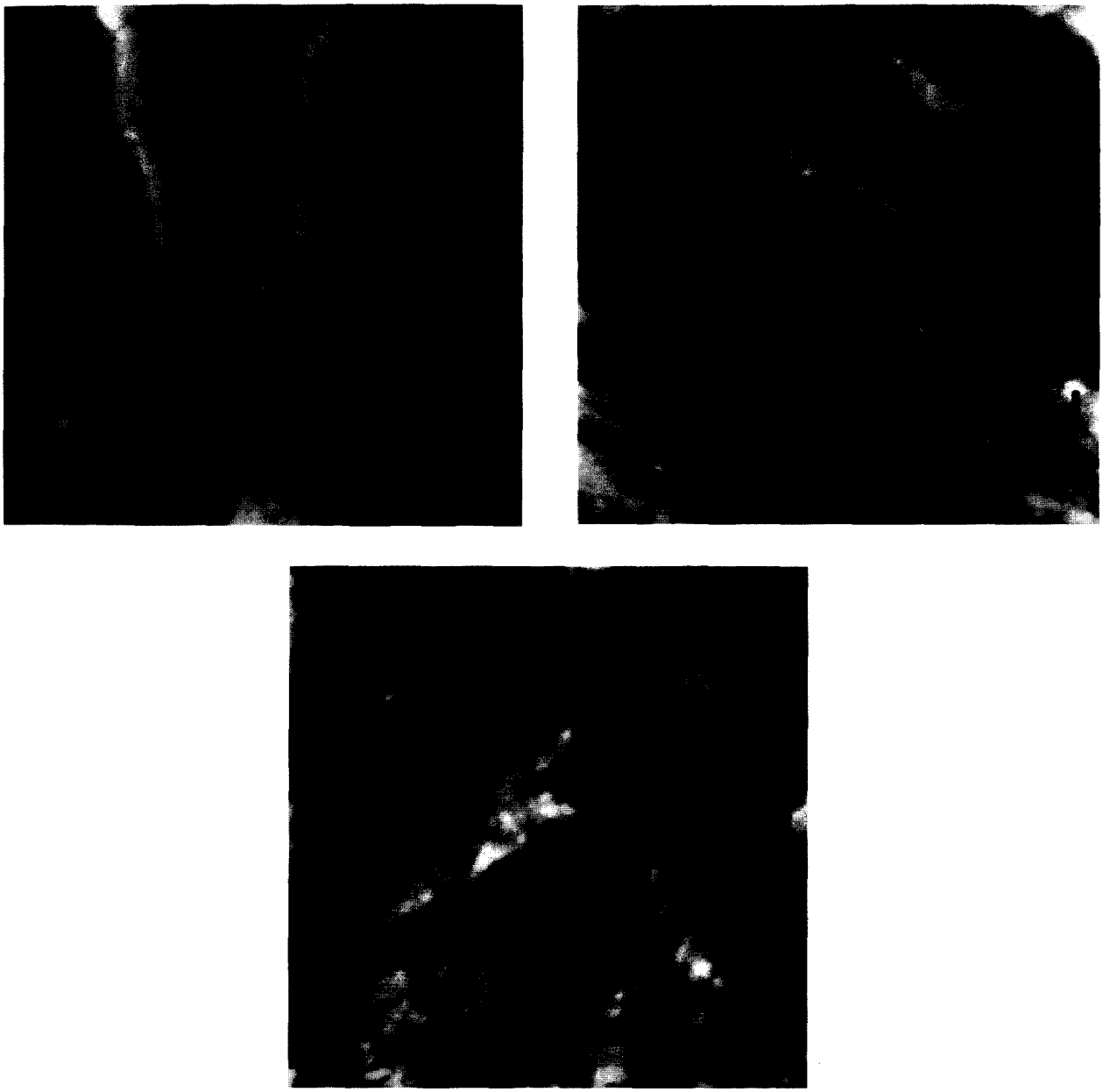

Fig. 12. iPP samples sheared at $\gamma = 1$: SFM images of the lamellar morphology in a spherulites. (a) The lamellae are parallel to the shear axis; (960 × 960 nm) image, z-range = 180 nm. (b) The lamellae are parallel to the principal tensile axis; (3 × 3 μm) image, z-range = 400 nm. (c) The lamellae are parallel to the principal compressive axis; (5 × 5 μm) image, z-range = 300 nm. The black arrows indicate the shear axes.

point of the 3D-spherulite, and Fig. 11 has to be considered as an archetype.

4.3. Lamellar morphology in deformed α spherulites

Fig. 12 shows three different lamellar morphologies corresponding to three different deformation states relative to the deformation ellipsoid.

The lamellar morphology, at $\gamma = 0.5$, is similar to the one in the undeformed state [26,36]. This is not very surprising since it has been shown previously that the local deformation of the α spherulites is less than in the β spherulites [22]. Likewise, the yield stress of a biphasic (monoclinic + hexagonal) polypropylene is lower than that of pure monoclinic polypropylene obtained by annealing a dual-phase sample. Thus, in all the SFM images of the α spherulites as those shown in Fig. 12, the actual local deformation is about 30–40% lower than in Fig. 11.

The salient features of Fig. 12 are globally the same as the ones observed in Fig. 11: no direct observation of intralamellar slip, but fragmentation (Fig. 12a,b) and kinking (Fig. 12c) of the radial lamellae. However, it has to be pointed out that: first, all the mechanisms are much less intense and cooperative than in the case of the β spherulites;

second, the daughter lamellae are no longer visible; and third, the crystalline lamellae are less resolved than in the undeformed case.

Finally, in contrast with earlier uniaxial tensile tests [22], during which macro-cavitation mechanisms were observed inside the α spherulites, here the plasticity is spread uniformly over the surface with rather diffuse damage as well.

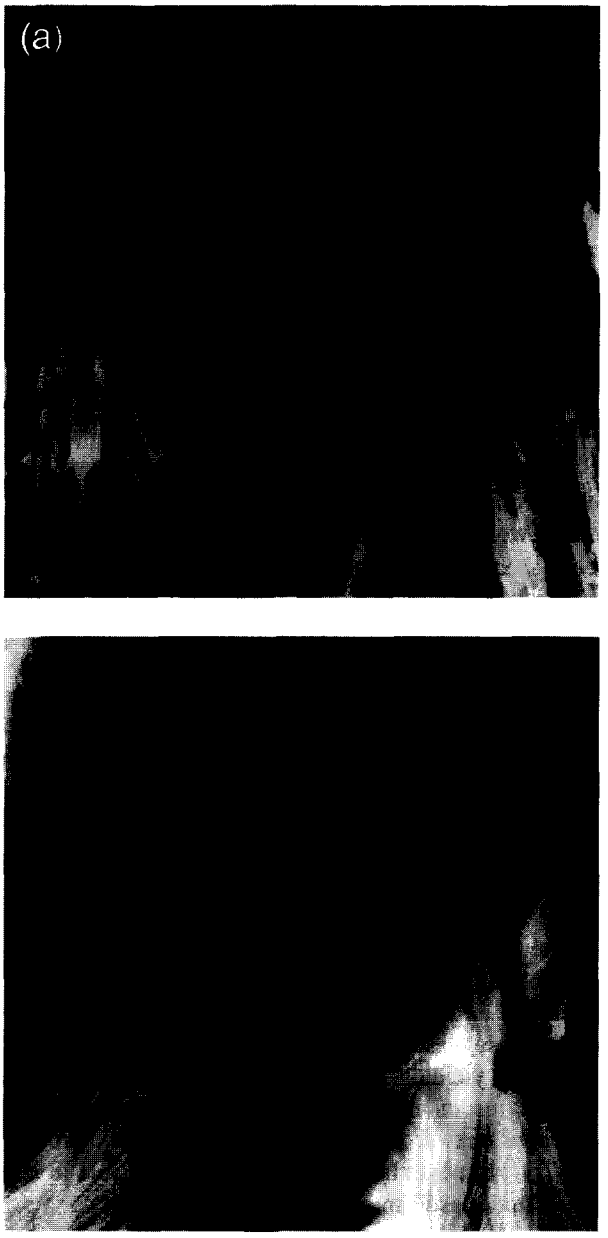

Fig. 13. Influence of the acid attack after the shear test up to $\gamma = 0.5$. Lamellar morphology in β spherulites. (a) Lamellae parallel to the shear axis: numerous pitting effects are seen in addition to the intralamellar fragmentations (5×5 μm) image, z-range = 800 nm. (b) Lamellae parallel to the principal compressive axis: lamellar kinkings, but in addition some lamellae are cut at the folds by the acid attack (4.5×4.5 μm) image, z-range = 1.2 μm. The black arrows indicate the shear axes.

4.4. Influence of the acid attack

All the SFM images shown here have been obtained with the following procedure: (1) first, the surface of the samples was etched in order to reveal the crystalline phase; (2) second, the sample was sheared; (3) third, the surface of the sheared sample was observed by SFM.

Some artefacts could be suspected from the chemical etching prior to deformation, such as: occurrence of nanocracks and loss of resolution at the lamellar level in the α phase. To make wholly clear this possible influence, shear tests have been performed on un-etched samples. The etching of the surface has been done prior to the SFM observation. No significant differences have been observed: nanocracks and kinks are still present. On the other hand, in addition to those previous mechanisms, numerous pits are seen on the whole surface (Fig. 13). Those pitting effects are due to a preferential attack of the acid in the damaged zones or in areas where the local stresses are large; this pitting effect is well-known in metallurgy and has been used to reveal the presence of dislocations [46]. As a consequence, the second procedure (shear followed by acid etching) has to be rejected.

5. Discussion

5.1. General overview of the plastic deformation of semi-crystalline polymers at temperatures $T_g < T_m$

Up to now, much experimental work has been devoted to the mechanical behaviour of semi-crystalline polymers at temperatures above the glass transition, so the amorphous phase is rubber-like: polyethylene [20,21], polypropylene [28,29], poly(ether ether ketone) [47], etc. Most of the investigations have been performed in the usual tensile mode; recently, there have been a few approaches using compressive or shear mode [20–22,28,29]. The influence of the applied stress on the microstructure (and vice versa) has been studied mainly by indirect techniques such as x-ray

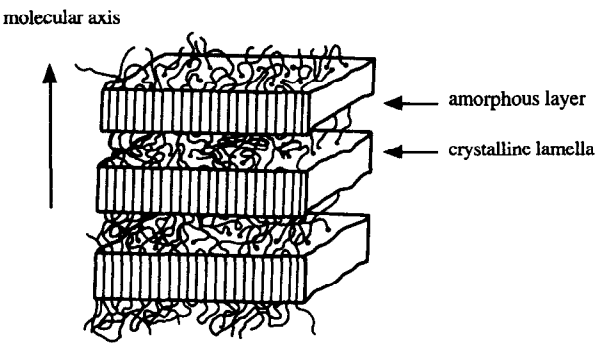

Fig. 14. Sketch of the basic crystalline microstructure of semicrystalline polymers. The chain axis within the crystalline lamellae lies along the thin direction. Between the lamellae, the amorphous layers contain chain ends, tie chains and fully included chains.

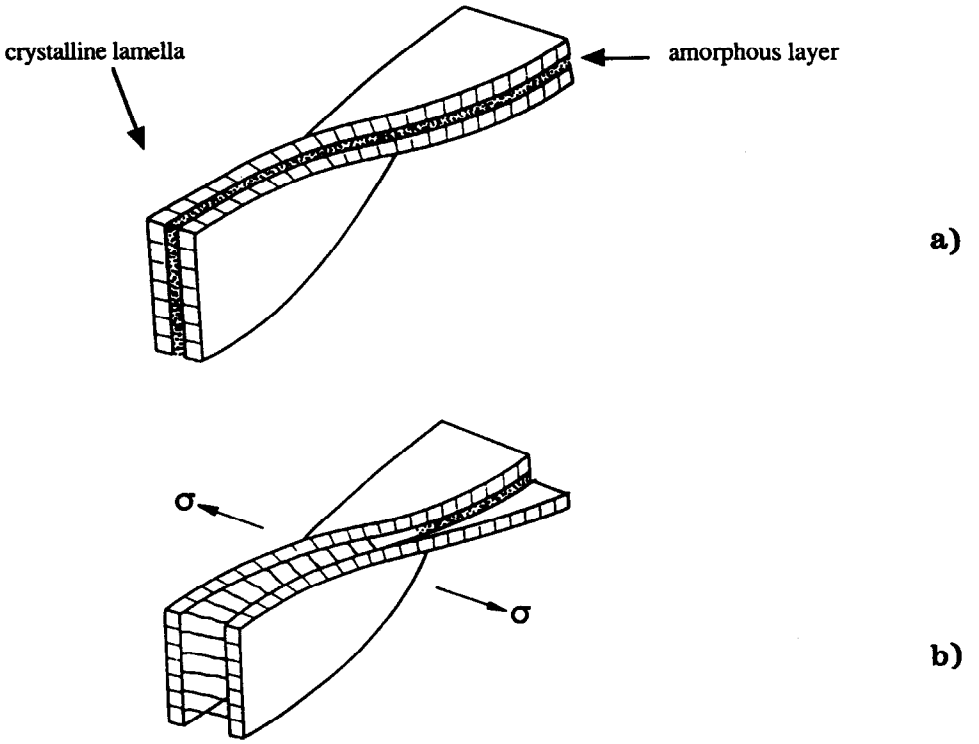

Fig. 15. Semicrystalline polymer ribbons twisting along their length. (a) No applied stress; (b) applied tensile stress perpendicular to the ribbon axis.

diffraction [13,20,21,47], differential scanning calorimetry (d.s.c.) [47], birefringence [11–16]. Very few direct observations of the microstructure of deformed semicrystalline polymers have been achieved at the lamellar level; the replication technique in TEM is rather tricky and does not allow in situ analysis. As reported above, scanning force microscopy is able to image the crystalline lamellae both in the undeformed state and in the deformed states.

A quantitative analysis of the local deformation mechanisms observed by SFM in Section 4 above requires a brief review of the main deformation mechanisms which have been deduced from previous experiments principally in HDPE under uniaxial tension.

The sketch of the basic crystallite microstructure of semicrystalline polymers is shown in Fig. 14. The amorphous layer consists of chain-end cilia, totally included chains and chains which are incorporated in two or more crystals (tie chains). Usually, the thin, ribbonlike crystals exhibit a regular twist about their long axis as shown in Fig. 15 [1,48]. The tie chains determine the continuity of the system and thereby control the level of elastic modulus [49], and can greatly affect the yield stress [50]. The crystals are elastically very anisotropic [51], with a much higher stiffness along the chain axis than in all the other directions. Thus, the orientation of the crystal in the stress field is very important in the elastic and plastic response to an applied load.

Before yielding, the deformation of the polymer results mainly from the deformation of the amorphous phase. The behaviour of each crystallite depends on its location within the spherulite and on its orientation relatively to the applied stress. Two basic modes have been reported: interlamellar shear (shear of the amorphous phase) and interlamellar separation (stretching or compression of the tie molecules) [11]. In the case of a twisted ribbonlike crystal structure (Fig. 15), it is worth noting that a tensile stress acting perpendicular to the growth axis of the lamellae will create elastic stretch of the tie molecules in the zones where the amorphous layers are perpendicular to the tensile axis and interlamellar shear where the amorphous layers are locally tangent to the tensile axis; it has been shown that both mechanisms have different relaxation times [52]. In HDPE, it has been reported that, beyond yielding, the sheared amorphous phase relaxes back much more slowly than the stretched one after unloading; furthermore, if the length of the sample is fixed constant during this slower relaxation, large local stresses develop and can lead to fracture as suggested by TEM observations [52].

Beyond yielding, the plasticity of semicrystalline polymers results mainly from the crystalline phase; the amorphous phase contributes very little to plastic processes ($T > T_g$), but nevertheless plays a significant role in stress transfer and plastic spin accommodation.

Like crystals of small molecules, polymer crystals can deform by slip, twinning or stress-induced martensitic transformation [6]. However, martensitic-like phase change and twinning do not contribute significantly to plastic strain but rather intervene in the transitory stages, bringing some crystals into an orientation more favourable for slip [53]. In contrast to crystals of small molecules, the number of

possible slip planes in polymer crystals is drastically limited, since the slip planes cannot cross the chain direction where the covalent bonds in the chain backbone strongly resist to deformation [2]. Two slip directions have been identified: (1) along the chain axis (chain slip) [11,17,54]; and (2) perpendicular to the chain axis (transverse slip) [13,53,55]. Chain slip is generally the easiest system to be activated.

Deformation by slip is usually governed by the resistance to the nucleation and glide of dislocations on the slip planes. The existence of dislocations in polymer crystals was evidenced in the 1960s and 1970s [56–58]. Peterson [59], pointing out that the lamellae are too thin for Frank–Read sources [46] to operate, proposed that plastic slip is mainly controlled by the nucleation of screw dislocations from the edges of the lamellar crystal under the effect of both a large local shear and thermal fluctuations. That model has been applied successfully by Young [60] to interpret the variation of the critical resolved shear stress of HDPE.

In bulk samples, most of the experimental studies have been focused on large plastic deformations obtained by uniaxial tension. From X-ray diffraction studies and few electron microscopy experiments, theoretical models have been proposed to explain the transformation of lamellae into microfibrils [8,9,61].

Concerning the above-mentioned intralamellar slip, Bowden and Young [6] have shown that chain slip in the same kind of planes can occur in two different ways to achieve the same macroscopic deformation: fine slip and coarse slip. In fine slip (Fig. 16a), a small amount of slip occurs equally on a large number of parallel planes; such slip results in a change of the angle between the chain axis and the normal to the lamellar surface. In coarse slip, a large amount of slip occurs on a few parallel planes only

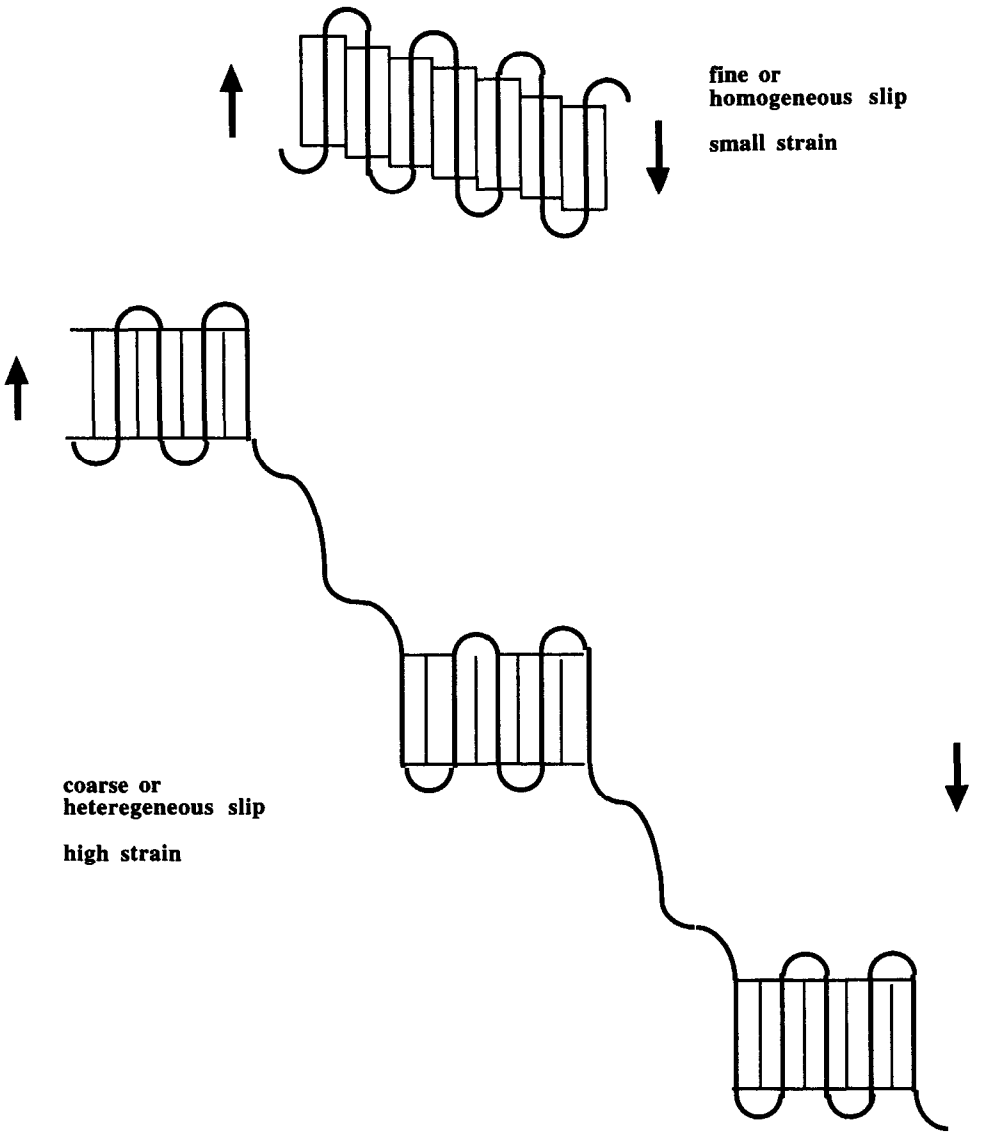

Fig. 16. Intralamellar slip: (a) fine slip, (b) coarse slip [6].

(Fig. 16b). The angle between the chain axis and the normal to the lamellar surface does not vary. Fine slip and coarse slip can operate competitively depending on the experimental conditions (deformation temperature, deformation mode).

In terms of dislocations, plastic yielding is considered to take its origin in the nucleation from the lateral crystal faces of pure screw dislocations parallel to the chain axis, which propagates through the crystal along (*hk*0) slip planes; fine slip is relevant to a homogeneous shear of the crystal lamellae thanks to the spreading of dislocation nucleation events over the entire length of the crystalline lamellae [54,62,63]. Brooks et al. [64] have shown that, after unloading ethylene–hexene copolymers from compressive experiments, low plastic strains are recoverable at room temperature. This recovery is consistent with an homogeneous shear of the lamellae [54] and with the back stress exerted by the distortion of the chain folds on the main surfaces of the sheared lamellae.

In contrast, coarse slip (or heterogeneous slip), which involves the fragmentation of the lamellae into blocks and the sliding process of blocks, is still less clear [65–68]. Recently, it has been shown [54] that, when polyethylene and ethylene copolymers are subjected to tensile load, both homogeneous and heterogeneous slip modes can operate in series association, the former being more thermally activated than the latter. Owing to its lower strain–hardening, activation of the heterogeneous slip may occur leading first to the fragmentation of the crystalline lamellae and then to the fibrillar texture including interfibrillar voiding.

Damage in deformed semicrystalline polymers were also reported. The most important features are: (i) the destruction of the crystalline lamellae into microfibrils observed in highly stretched polymers [8,47,61]; severe fragmentations of crystalline lamellae have also been reported by Galeski et al. in HDPE deformed by plane strain compression at large plastic strains [65], (ii) the micro-cavitation related to locally extensive drawing of the polymer [69]; such micro-cavitation is suspected to occur within highly stretched amorphous layers [70,71]; (iii) the crazes in micronecks which transform the folded-chain lamellae into the fibrillar structure [19]; and (iv) in uniaxial compressive tests, the kinking of crystalline lamellae which lie parallel to the compression axis [20].

5.2. Deformation mechanisms observed by SFM in sheared isotactic polypropylene

Before discussing the evolution of the lamellar morphology in sheared polypropylene, it is important to recall that all the SFM observations of the surface of the sheared sample have been performed after having unloaded the sample.

As mentioned in Section 4, no trace of localized intralamellar slip has been detected even when the crystalline lamellae lie perpendicular to the shear axis (Fig. 11b); i.e. when the Schmid factor is maximum. When the strain level is low ($\gamma = 0.5$), the lamellae look unchanged relative to the undeformed state. This observation does not mean that there is no intralamellar slip; rather it suggests either that the slip is homogeneous within the crystalline lamellae under loading or, as has been previously observed in polyethylene and related copolymers [54,64], that the slip is totally reversible upon unloading. Here, in the case of sheared polypropylene, the recovery of the total deformation of the sample after unloading is about 40% which is consistent with the existence of homogeneous slip. As a consequence, after unloading, the lamellae come back to their initial morphology as shown in Fig. 17. When increasing the strain level up to $\gamma = 1$, fragmentation of the lamellae is frequent

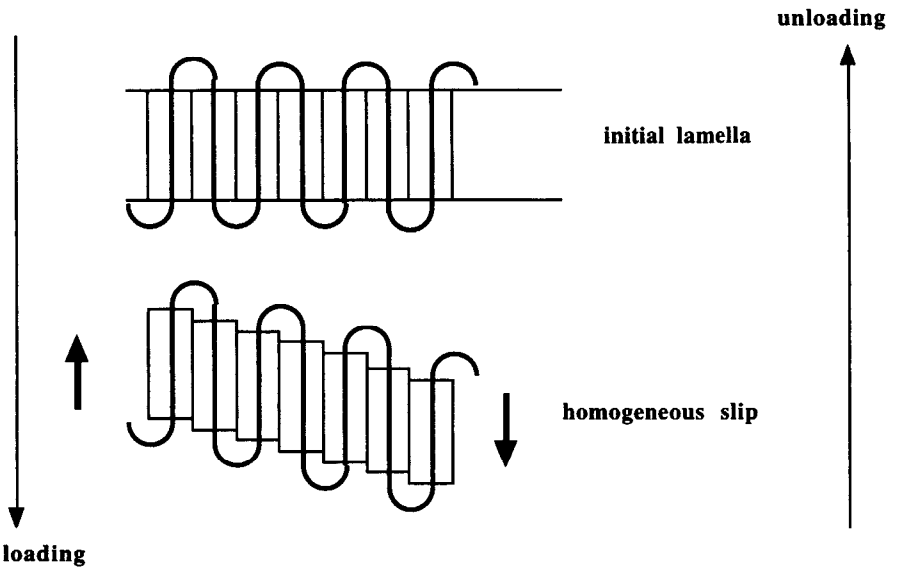

Fig. 17. Fine (homogeneous) intralamellar slip, evolution of the lamellar morphology: (1) upon loading; (2) upon unloading. The short black arrows indicate the shear directions while loading.

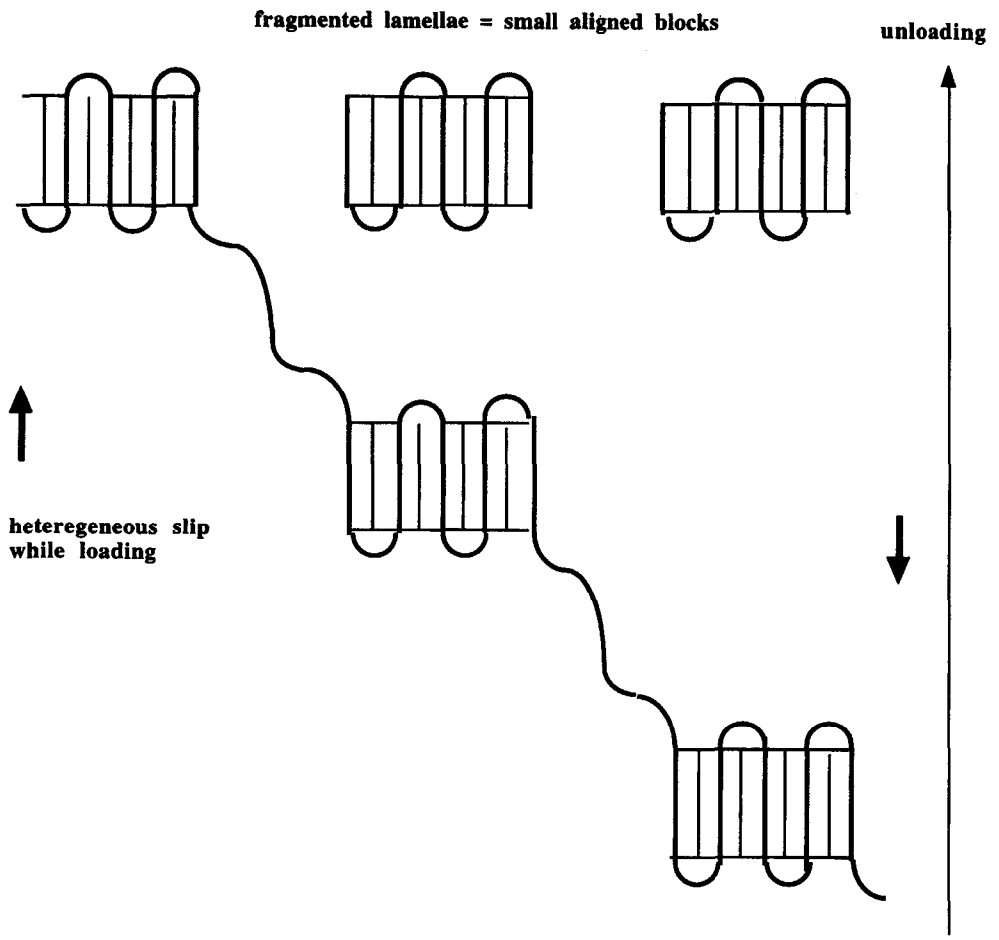

Fig. 18. Coarse (heterogeneous) intralamellar slip, evolution of the lamellar morphology: (1) upon loading; (2) upon unloading. The short black arrows indicate the shear directions while loading.

and the lamellae are broken into smaller aligned blocks (Fig. 11b). This form of damage is easily explained if heterogeneous slip takes place in the lamellae while loading the sample. As the load is removed, the connecting extended rubbery chains between the blocks tend to relax and the lamellae eventually adopt the morphology shown in Fig. 18. Our observations suggest that homogeneous slip precedes heterogeneous slip; it agrees with previous studies which have shown that both modes can operate in series association [54,72].

When the lamellae are parallel to the shear axis, no intralamellar slip was observed (Fig. 11a). This is not surprising since the slip plane is perpendicular to the shear axis whatever the shape of the lamellae (twisted or straight); the Schmid factor is thus equal to zero and intralamellar slip is not expected. In contrast, depending on the orientation of the lamellar surfaces relative to the applied shear plane, interlamellar shear should occur during the loading of the sample. In the case of twisted lamellae (Fig. 15a), shear of the tie molecules within the amorphous layers is easy when the lamellar surfaces are perpendicular to the applied shear plane; on the contrary, when the surfaces of the lamellae are parallel to the shear plane (90° twist), the applied shear stress has no effect on the amorphous layer. In other words, along a twisted lamellae whose helicoidal axis is parallel to the applied shear, there will be alternatively sheared amorphous layers and unsheared ones; as a consequence, large local strains should develop within the amorphous phase. The lamellar morphology shown in Fig. 11a corroborates this interpretation: numerous fragmentations of the crystalline lamellae are seen at a strain level $\gamma = 1$ (while there are only few at $\gamma = 0.5$), they are perpendicular to the lamellae. Their presence could result from the large local strains developed in the amorphous layer during the loading or from their relaxation during the unloading. Previous studies have shown that such strains can be sufficient to rupture the material [52]. It is reasonable to think that the fragmentations occur at those points where the tie molecules emerge from the crystal face: the load becomes concentrated in those points. Since it is well-known that the density of tie molecules decreases as the time of crystallization increases [50], the number of fragmentations should depend on the kinetics of crystallization.

When the orientation of the crystalline lamellae is such that their direction of growth is parallel to the principal tensile strain axis, few cooperative nanocracks go through

stacks of lamellae at $\gamma = 0.5$, the nanocracks are perpendicular to the tensile axis. At $\gamma = 1$, the number of collective nanocracks increases dramatically (Fig. 11c), their width is about 100 nm and their length can reach several microns. Those thin nanocracks are different from the cracks which occur in uniaxial tensile tests [22]; in the latter case, the cracks are much larger because of the dilating stress field. If a stack of lamellae which are parallel to the tensile axis is surrounded by other stacks of lamellae which are not parallel to the tensile axis, that stack is broken into smaller lamellar blocks [26]; that behaviour results from the addition of local internal stresses due to the neighbouring stacks to the applied shear.

Finally, when the lamellae lie along the principal compressive axis, collective kinking of the lamellae has been observed (Fig. 11d) and, at $\gamma = 1$, kink bands are formed. That behaviour has been already encountered in HDPE under uniaxial compression [20] and plane–strain compression [65] at room temperature; the kink bands have been observed in the bulk by transmission electron microscopy [20]. Bartczak et al. [20] mentioned that kinking in lamellae lying parallel to the compression axis was at the origin of the fine shear bands. They noticed that the formation of kinks was the only discontinuous transformation during the whole deformation process and it was limited to the small fraction of suitably oriented crystallites. However, that mechanism is not completely understood. It could result from the presence of the amorphous, rubbery phase; under compression, such an incompressible rubbery phase is expected to develop large internal stresses, the kinks could be formed by relaxation of those internal stresses.

Most of the above discussion has been focused on the evolution of the lamellar morphology of the β spherulites. However, our data show clearly that the deformation mechanisms are much less intense in the α spherulites than in the β ones. In a previous paper [22], uniaxial tensile tests performed on the same samples have shown that, at the spherulitic scale, the α spherulites were brittle, while the β ones were ductile: at early stages of deformation, cavitation occurs at the α spherulites boundaries and at their equatorial region perpendicular to the tensile axis, while diffuse crazing appears in β spherulites at large strains. On the other hand, it was pointed out that, in simple shear tests, at the same spherulitic level, both α and β spherulites were able to undergo large plastic deformation. However, the SFM micrographs we have presented here at the lamellar level show that, even if the local mechanisms are basically the same for both α and β spherulites, there are some differences due to the presence of the daughter lamellae in the former case. In α spherulites, the mechanisms are less intense then in the β phase: kinking of the radial lamellae is not cooperative and kink bands do not spread over the surface as observed in β spherulites (Fig. 12c); there are no cooperative nanocracks perpendicular to the principal tensile axis going through stacks of lamellae, but rather localized fragmentations of the radial lamellae (Fig. 12b). A partial explanation could be that the local deformation of the α spherulites is less than that of the β ones [22].

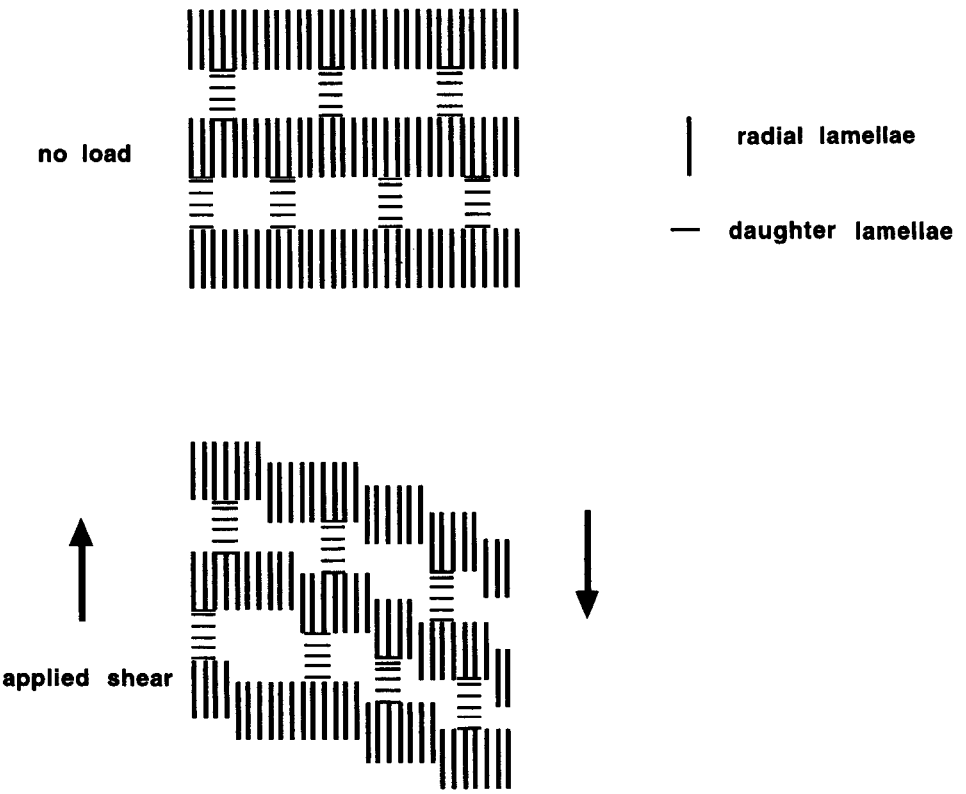

Fig. 19. One possible model for the shearing of the radial/daughter lamellar network in α spherulites.

However, it is essential to take account of the existence of the daughter lamellae in the development of plasticity in the crystalline phase. As mentioned above, beyond yielding, the plasticity of the semicrystalline polymer results mainly from the crystalline phase. The major deformation mechanism involved in plastic deformation is the intramellar slip which is governed by the resistance to the motion of dislocations in the slip planes. In isotactic polypropylene, dislocations are capable of gliding only in planes containing the chain axis **c**. In the monoclinic α phase, the possible slip systems, according to an increasing critical resolved shear stress (CRSS), are the (010) [001], (100) [001], (110) [001], (110) [001] chain slip systems and the (001) [100] transverse slip systems [22]. The easiest slip system is thus the (010) [001] one. If we refer to Fig. 10a, the 3D-architecture of the α phase is complex and the propagation of dislocations within that crystalline architecture is not straightforward. Indeed, let us suppose that chain slip is initiated in a radial lamella along the easiest (010) [001] slip system; its propagation into a daughter lamella requires the continuity of both the slip plane and the slip direction; however, in a daughter lamella, the (010) [001] slip system corresponds to a transverse slip which is not energetically favourable. If we consider now that chain slip starts in a radial lamella along the second easy (100) [001] system; slip should continue along the (001) [100] system of the daughter lamella and should thus lead to cutting of the chains, which is unlikely. In other words, the propagation of dislocations through the crystalline phase will be possible only along a sinuous path such as the one shown in Fig. 19, and the ability for plastic deformation is thus reduced. It is also important to point out that, in the 3D-architecture of the α phase, the amorphous rubbery phase is confined to certain types of compartments; interlamellar shear (or separation) seem difficult and the role played by the amorphous phase is not evident.

Finally, it is worth noting that, in Fig. 12, the daughter lamellae have lost their visibility and only the radial ones can be seen any longer. That phenomenon has been observed systematically in the α spherulites sheared up to $\gamma = 1$. To date, no definite model is available to explain the 'disappearance' of the daughter lamellae. A possible cause could be that the angle between radial and daughter lamellae has changed because of the applied shear, and that the daughter lamellae are pulled over to the radial lamellae. Since the surface roughness is about twice that of the undeformed sample, the resolution is less and, consequently, it is not possible to distinguish the short daughter lamellae from the radial ones [26]. A way to check that assumption would be, for example, to shear an α_I type-monocrystal and to follow by SFM the evolution of the daughter lamellae with the deformation. Another way would be to study by SFM the lamellar morphology of α_{II} spherulites relative to the applied shear stress. Indeed, in that kind of spherulite, the number of daughter lamellae varies with the crystallization temperature T_c; starting with a small number of daughter lamellae (high T_c), it could be easier to understand the influence of the daughter lamellae and then to go deeper into the study by progressively increasing the number of the daughter lamellae.

6. Conclusion

In the specific case of intruded iPP samples deformed under applied shear stress, we have shown that scanning force microscopy is able to image directly the plasticity and damage mechanisms at the lamellar level inside each kind of spherulite. Two levels of permanent shear strain ($\gamma = 0.5$ and 1) have been investigated. The SFM micrographs show clearly that, even if the local mechanisms are basically the same for both α and β spherulites, their intensity is much less low in the α spherulites than in the β ones due to the presence of the daughter lamellae in the former case. The main deformation mechanisms which have been observed are the following: (i) kinking of the lamellae which lie along the principal compressive axis; (ii) nanocracks across the lamellae lying along the principal tensile axis; (iii) fragmentations of the lamellae which are parallel to the shear axis; (iv) at low strain level, no fragmentations of the lamellae which are perpendicular to the shear axis; but fragmentations of the lamellae at higher strains. No intralamellar slip has been directly observed.

However, as has been mentioned above, all the SFM observations have been performed after unloading the sample. As the rubbery amorphous phase relaxes during the unloading, the SFM micrographs show the evolution of the lamellar morphology which results from both the loading and the unloading. In order to get rid of the relaxation of the rubbery amorphous phase, in situ SFM experiments are in progress. Those experiments could help us to answer to opened questions such as: (i) does homogeneous intralamellar slip occur at low strain level? (ii) Is heterogeneous intralamellar slip predominant at higher strains? (iii) Does the lamellar kinking occur during the loading or the unloading? (iv) Are the fragmentations observed in the lamellae lying parallel to the shear axis due to interlamellar slip?

On the other hand, in the intruded iPP samples under study, a straightforward relationship between the observed deformation mechanisms and the applied shear stress has not been obvious. Indeed, those samples contain both α and β spherulites in equal quantity. Furthermore, the α spherulites deform less than the β ones. In other words, the local stress is not expected to reflect the applied shear stress and the analysis of the observed deformation mechanisms is not easy. In a future study, we intend to study monophasic α or β iPP separately.

The behaviour of the α phase is still obscure, and the influence of the daughter lamellae on the local deformation mechanisms is unresolved. One way to clarify that influence is to study monophasic an iPP isothermally crystallized at

different temperatures: at high temperatures (about 160°C), α spherulites contain radial lamellae only; when decreasing the crystallization temperature, daughter lamellae start to grow. Thus, we plan to study the local deformation mechanisms *versus* an increasing number of daughter lamellae.

Acknowledgements

The authors are very grateful to R. Séguéla (LSPES, USTLille, France) and to B. Lotz (ICS, Strasbourg, France) for several illuminating discussions. This research was supported in part by the Contrat de Plan Etat-Région 1994–1999, by the FEDER (CEE program) and by the Ministère de l'Enseignement Supérieur et de la Recherche.

References

[1] Bassett DC. Principles of polymer morphology. Cambridge: Cambridge University Press, 1981.
[2] Haudin J-M. In: Escaig B, G'Sell C, editors. Plastic deformation of amorphous and semicrystalline materials. Les Ulis, France: Les Editions de Physique, 1979:291–311.
[3] Schultz JM. Polym Eng Sci 1974;24:770.
[4] Natta G, Corradini P, Cesari M. Rend Acad Naz Lincei 1956;21:365.
[5] Padden FJ, Keith HD. J Appl Phys 1959;30:1479.
[6] Bowden PB, Young RJ. J Mater Sci 1974;9:2034.
[7] Peterson JM. J Appl Phys 1966;37:4047.
[8] Peterlin A. J Mater Sci 1971;6:490.
[9] Petermann J, Kluge W, Gleiter H. J Polym Sci Polym Phys Ed 1979;17:1043.
[10] Wang TT. J Polym Sci Polym Phys Ed 1974;12:145.
[11] Young RJ, Bowden PB, Ritchie JM, Rider JG. J Mater Sci 1973;8:23.
[12] Pope DP, Keller A. J Polym Sci Polym Phys Ed 1975;13:533.
[13] Lin L, Argon AS. Macromolecules 1992;25:4011.
[14] Gaucher-Miri V, François P, Séguéla R. J Polym Sci Polym Phys Ed 1996;34:1113.
[15] Hay IL, Keller A. Kolloid Zuz Polymere 1965;204:43.
[16] Weynant E, Haudin J-M, G'Sell C. J Mater Sci 1980;15:2677.
[17] Gleiter H, Argon AS. Phil Mag 1971;24:71.
[18] Allan P, Bevis M. Phil Mag 1980;41:555.
[19] Geil PH. Polymer single crystals. New York: Interscience, 1963.
[20] Bartczak Z, Cohen RE, Argon AS. Macromolecules 1992;25:4692.
[21] Bartczak Z, Argon AS, Cohen RE. Macromolecules 1994;35:3427.
[22] Aboulfaraj M, G'Sell C, Ulrich B, Dahoun A. Polymer 1995;36:731.
[23] Snétivy D, Vancso GJ. Polymer 1994;35:461.
[24] Cramer K, Schneider M, Mulhaupt R, Cantow HJ, Magonov SN. Polym Bull 1994;32:637.
[25] Hild S, Gutmannsbauer W, Luthi R, Fuhrmann J, Guntherodt H-J. J Polym Sci Polym Phys Ed 1996;34:1953.
[26] Castelein G, Coulon G, G'Sell C. Polym Eng Sci 1997;37:1694.
[27] Ward IM. Mechanical properties of polymers. New York: Halsted Press–Wiley, 1975.
[28] Porzucek K, Coulon G, Lefebvre JM, Escaig B. J Mater Sci 1989;24:2533.
[29] Porzucek K, Lefebvre JM, Coulon G, Escaig B. J Mater Sci 1989;24:3154.
[30] Collin B, Chatenay D, Coulon G, Ausserré D, Gallot Y. Macromolecules 1992;25:1621.
[31] Maaloum M, Ausserré D, Chatenay D, Coulon G, Gallot Y. Phys Rev Lett 1992;68:1575.
[32] Bourdieu L, Maaloum M, Silberzan P, Ausserré D, Coulon G, Chatenay D. Ann Chim Fr 1992;17:229.
[33] Stocker W, Graff S, Lang J, Wittman J-C, Lotz B. Macromolecules 1994;27:6677.
[34] Binnig G, Quate CF, Gerber C. Phys Rev Lett 1986;12:930.
[35] Digital Instruments, Nanoscope III, scanning probe microscopes, instruction manual. Santa Barbara, CA: Digital Instruments.
[36] Castelein G, Coulon G, Aboulfaraj M, G'Sell C, Lepleux E. J Phys III France 1995;5:547.
[37] Aboulfaraj M, Ulrich B, Dahoun A, G'Sell C. Polymer 1993;34:4817.
[38] Olley RH, Bassett DC. Polymer 1982;23:1707.
[39] G'Sell C, Hiver J-M, Dahoun A, Souahi A. J Mater Sci 1992;27:5031.
[40] Wunderlich B. In: Macromolecular physics, vol. 1, crystal structure, morphology, defects. New York: Academic Press, 1973.
[41] Norton DR, Keller A. Polymer 1985;26:704.
[42] Castelein G. Thèse de Doctorat de l'Université des Sciences et Thechnologies de Lille, 1996.
[43] Khoury F. J Res Natl Bur Stand 1966;A70:29.
[44] Lotz B, Wittmann J-C. J Polym Sci Polym Phys Ed 1986;24:1541.
[45] Bassett DC, Vaughan AS. Polymer 1985;26:717.
[46] Hull D, Bacon DJ. Introduction to dislocations, 3rd edn. Oxford: Pergamon Press, 1984.
[47] Dahoun A, Aboulfaraj M, G'Sell C, Molinari A, Canova GR. Polym Eng Sci 1995;35:317.
[48] Fischer ED. Z Naturforschung 1957;12A:753.
[49] Kriegbaum WR. J Polym Sci 1966;15C:251.
[50] McCready MJ, Schultz JM, Lin JS, Hendricks RW. J Polym Sci Polym Phys Ed 1979;17:725.
[51] McCullough RL. In Schultz JM, editor. Treatise on materials science, vol. 10B, properties of solid polymeric materials. New York: Academic Press, 1977.
[52] Petermann J, Schultz JM. J Mater Sci 1978;13:50.
[53] Frank FC, Keller A, O'Connor A. Phil Mag 1958;3:64.
[54] Gaucher-Miri V, Séguéla R. Macromolecules 1997;30:1158.
[55] Keller A. J Polym Sci 1956;21:363.
[56] Petermann J, Gleiter H. Phil Mag 1972;25:813.
[57] Keith HD, Passaglia E. J Res Natl Bur Stand 1964;68A:513.
[58] Predecki P, Statton WO. Appl Polym Symp 1967;6:165.
[59] Peterson JM. J Appl Phys 1966;37:4047.
[60] Young RJ. Phil Mag 1974;30:85.
[61] Schultz JM. Polymer materials science. Englewood Cliffs, NJ: Prenctice Hall, 1974:496.
[62] Young RJ. J Mater Forum 1988;11:210.
[63] Crist B, Fisher C, Howard PR. Macromolecules 1989;22:1709.
[64] Brooks NW, Duckett RA, Ward IM. Polymer 1992;33:1872.
[65] Galeski A, Bartczak Z, Argon A, Cohen RE. Macromolecules 1992;25:5705.
[66] Peterlin A, Meinel G. Makromol Chem 1971;142:227.
[67] Takayanagi M, Kajiyama T. J Macromol Sci Phys Ed 1973;8:23.
[68] Thomas EL, Sass SL, Kramer EJ. J Polym Sci Polym Phys Ed 1974;12:1015.
[69] Friedrich K. In: Kausch HH, editor. Advances in polymer science. Berlin: Springer-Verlag, 1983.
[70] Peterlin A. Polym Eng Sci 1979;19:118.
[71] Lin L, Argon AS. J Mater Sci 1994;29:294.
[72] Burnay SG, Daere MD, Groves GW. J Mater Sci 1978;13:639.